RESEARCH ARTICLE

ADVANCED FUNCTIONAL MATERIALS
www.afm-journal.de

Electrical Impedance Tomography Monitoring of Salt Transportation in Cellulose Hydrogel for Solar-Driven Evaporative Desalination via Laser Defined Wettability

*Yang Xu, Haosong Zhong, Xupeng Lu, Miao Tang, Siyu Chen, Cuiyun Yang, Yi Chen, Minseong Kim, Yang Liu, and Mitch Guijun Li**

The scarcity of clean water has become a growing problem worldwide. Solar-driven desalination based on evaporation has become a promising green technology for obtaining drinking water from saline water for the welfare of human society. However, the accumulation of salt precipitated from the saline at the evaporator surface remains a severe problem in improving evaporation efficiency. To overcome this problem, it is crucial to investigate the transportation mechanism of salt in the saline during the evaporation process. Herein, an in situ monitoring strategy with the electrical impedance tomography (EIT) method is proposed to characterize the salt transportation and accumulation process inside the nano-crystal cellulose (NCC)-MnO_2 nanoparticle solar evaporator. The coating of laser-induced graphene (LIG) with tunable water wettability shows that the hydrophobic structures can suppress salt accumulation during evaporation. The collected condensation water generated from the bacteria-polluted saline proves to be clean. It is hoped that this work can further inspire research on the salt-resistive evaporator design.

1. Introduction

Clean and fresh water, which is essential to human living and industrial prosperity, has become a more and more precious resource due to the growing shortage across the world.[1] Despite the vast amount of total water reserves, freshwater takes a tiny portion of it, while most of the water cannot be utilized directly. There have been various methods to generate fresh water from unusable sources like seawater, wastewater, or even the atmosphere. Commonly used water generation technologies include membrane-based and evaporation-based water generation, as well as adsorption-based atmospheric water capture. Membrane-based water desalination technology like osmosis usually requires professional and expensive devices, high power consumption, frequent maintenance, and pre-treatment of the water source,[2] making it difficult to promote for developing countries and areas. Atmospherical water harvesting (AWH) consumes nearly zero power, and the ingredients are usually cheap, but the throughput is limited.[3] Evaporation-based water desalination technologies enjoy the benefits of cost-effective devices and comparatively high clean water throughput, which includes active and passive water vapor generation. However, the active water vapor generation method, like heating, still costs a large amount of energy. At the same time, solar light is a free and clean energy source that can be exploited for evaporation.

Solar light has a mean power density of 1000 W m^{-2} at the sea level of Earth after passing through the atmosphere.[4] The solar irradiance spectrum delivered to Earth after passing through the atmosphere remains mostly within the 0.25 μm to 2.5 μm range due to the absorption of various molecules, including carbon

---

Y. Xu, H. Zhong, X. Lu, M. Tang, S. Chen, C. Yang, Y. Chen, M. Kim, M. G. Li
Center for Smart Manufacturing
Division of Integrative Systems and Design
The Hong Kong University of Science and Technology
Clear Water Bay, Kowloon, Hong Kong SAR 999077, China
E-mail: mitchli@ust.hk

The ORCID identification number(s) for the author(s) of this article can be found under https://doi.org/10.1002/adfm.202425052

DOI: 10.1002/adfm.202425052

Y. Liu
Department of Applied Physics
The Hong Kong Polytechnic University
Kowloon, Hong Kong SAR 999077, China

M. G. Li
Hong Kong Branch of Chinese National Engineering Research Center for Tissue Restoration and Reconstruction
The Hong Kong University of Science and Technology
Clear Water Bay, Kowloon, Hong Kong SAR 999077, China

M. G. Li
Joint Laboratory for Wave Functional Materials Research
The Hong Kong University of Science and Technology
Clear Water Bay, Kowloon, Hong Kong SAR 999077, China

dioxide, water, and ozone. However, the water does not absorb heavily within this solar irradiance spectrum range.[5] The energy from the sun can travel for some distance and reach deep into the bulky water. The heat generated from the solar light eventually gets dissipated in such bulky water, making the evaporation of water insignificant. Therefore, it is necessary to enhance the absorption of solar light and the interfacial evaporation of the water to improve the photothermally-induced water vapor generation.[6] Researchers analyzed the different conditions of water evaporation from bottom or bulky heating to interfacial heating with planar and three-dimensional configurations to further push forward the evaporation efficiency.[7] The improved interfaces between the top and bulky water as well as between wet water and dry evaporator will both promote evaporation, such as some capillary surface on metals or porous absorbers.[8] Many researchers have paid attention to improving interfacial water evaporation efficiency by introducing broadband spectrum absorbers,[9,10] engineering micro-structures and nano-structures,[11–13] and improving water transportation channel efficiency[14–16] or heat transportation pathway.[17,18] However, a key problem lies on the road to the massive application of solar-driven desalination, which is the accumulation of crystalline salt after water is evaporated from the saline water.[19] Researchers pointed out that the microstructures of the evaporator are vulnerable to being blocked or covered by the salt crystals formed during the evaporation which reduces the evaporation efficiency.[20] Various methods have been proposed to fight against the accumulation of salt by porous structures, hydrophobic materials, and mechanical responses.[21–24] Some novel evaporators show good anti-salt performances using multiple strategies by the highly absorptive porous materials and the self-rolling sphere structure to remove the salt instantly.[25] On the other hand, the precipitated salt can be useful for the collection of certain elements like lithium from the waste brine water.[26–28] Therefore, it is necessary to investigate more on the salt transportation in the photothermal evaporator. However, the understanding of the transportation mechanism of salt and saline water within the solar evaporation process is lacking. It would help us design better salt-resistive materials and structures if we could further investigate the transportation process.

Hydrogel has been used in water transport, storage, and capture due to its microstructures and hydrophilic properties.[29,30] Hydrogel formed with either physically or chemically cross-linked molecular networks like sodium alginate, poly(acrylic acid), and nano-cellulose can bond with water molecules and form a transport channel that boosts the adsorption and movement of water.[31–33] Many researchers proposed the applications of hydrogel in solar-driven water evaporation because of their good performance in water transportation.[34–36] Nano-crystal cellulose (NCC) manufactured from wood can be used as an excellent green precursor for cellulose-based hydrogel/aerogel without involving redundant chemical wastes.

Electrical impedance tomography (EIT) has been used in the non-invasive detection of fluids, like multi-phase flow or biomedical inspections.[37] The peripheral electrodes forming a closed circular loop can stimulate weak electrical currents and measure the induced voltage signals sequentially. The electrical conductivity of the inner area within the electrode array can be, therefore, reconstructed with specific algorithms. The EIT measuring is sensitive to changes in conductivity, either in spatial distribution or concentration. Therefore, it can achieve real-time sensing and tomographic imaging of the target area without leading to any damage, allowing it to become an excellent tool for detecting delicate or biological samples.[38] EIT technology has been widely utilized in areas such as clinic diagnosis, human-machine interaction, and industrial process monitoring.[39–41] Some researchers reported the successful EIT monitoring of the water adsorption process of the atmospheric water harvesting process.[42,43] However, there is still a scarcity of research concerning real-time monitoring of salt transportation in solar evaporation using EIT technology.

Herein, we propose a cellulose-hydrogel evaporation device with a tunable superhydrophilic/superhydrophobic solar absorber by mixing MnO_2 nanoparticles with the NCC hydrogel together with the deposition of superhydrophilic/superhydrophobic laser-induced graphene (LIG) nanoparticle layer to achieve the in situ monitoring of the salt transportation with the help of EIT, as shown in **Figure 1**. The monitored salt concentration shows a directional movement towards the superhydrophilic area of the evaporator due to the evaporation-driven water flow. The bacteria incubation tests show absolutely no bacteria contamination detected in the collected condensed water after evaporation from the simulated polluted saline.

2. Results and Discussion

2.1. Fabrication and Characterization

The nano-crystal cellulose obtained from the physical breakdown and chemical hydrolysis process of the natural wood forms a 15 wt% suspension in water. The NCC suspension acts as a suitable substrate for loading functional light-absorbing materials like metal oxide nanoparticles (NPs) or carbonic materials such as laser-induced graphene or carbon black (CB).[44,45] The NCC is dispersed in the water in a non-homogeneous state as it tends to form a cross-linked network spontaneously. In order to make it possible for the functional materials to be loaded into the molecular skeleton more efficiently, ultrasound sonication is needed to break the cross-linked networks. After the sonication, MnO_2 powder is added, and the second round of sonication is applied to mix the MnO_2 nanoparticles with the NCC hydrogel to achieve a uniformly dispersed NCC-MnO_2 suspension.

The as-prepared NCC-MnO_2 suspension is dark and capable of absorbing solar irradiation. However, the excess water remaining inside the suspension not only weakens the bonding between the NCC and MnO_2 NPs but also hinders the energy-absorbing process as the relatively thick and bulky water membrane absorbs the solar light before it can reach the bottom interfacial photothermal materials. Therefore, we use the freeze-drying method to remove obsolete water in the NCC-MnO_2 mixture to create a dry and porous cellulose aerogel. We freeze the mixture in the freezer at −18 °C for 2 h until it is fully frozen. After that, we put the frozen solid mixture into the vacuum freeze-drying machine for 24 h to get the NCC-MnO_2 aerogel. It is worth noting that since the NCC-MnO_2 has a strong light absorption, we can reduce the usage of MnO_2 by depositing one thin layer of the NCC-MnO_2

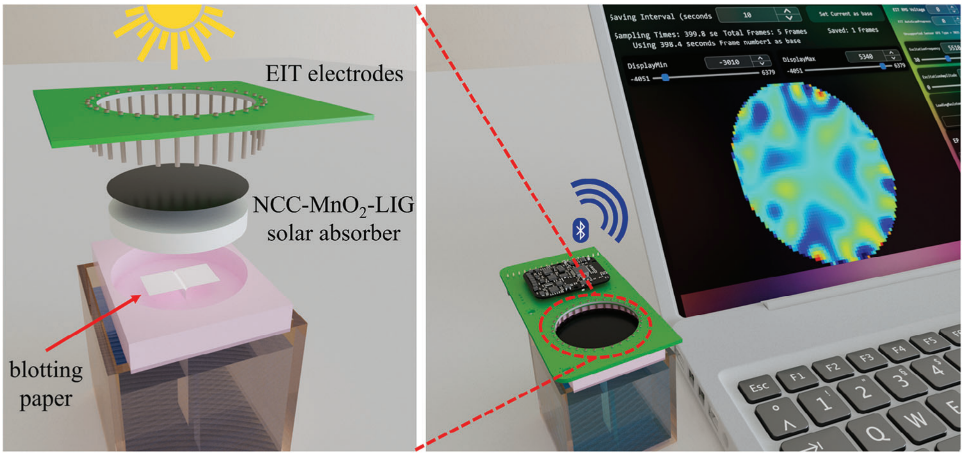

Figure 1. The illustration of the solar-driven evaporation device with EIT monitoring of the salt water transportation within the $NCC-MnO_2-LIG$ absorber and the data collection and transmitting scheme enabled by the home-designed printed circuit board devices.

onto the pristine NCC suspension before we send the composite for freeze-drying, as shown in **Figure** 2a.

After freeze-drying, the porous $NCC-MnO_2$ aerogel is cut and loaded into the 3D-printed evaporation container with a thin water transportation channel made of a piece of blotting paper that can easily absorb water. Then, the evaporator is inserted into a deionized (DI) or saline water container so that the bottom water transportation channel can get in touch with the water. The device is kept for 15 min to let the dry $NCC-MnO_2$-LIG aerogel absorb water by the capillary effect until the surface is wet before we deposit laser-induced graphene (LIG) on the top surface of the $NCC-MnO_2$ evaporator with a 1064 nm fiber laser. After the LIG deposition, the completed $NCC-MnO_2$-LIG evaporator is put under the simulated solar lamp for evaporation.

The $NCC-MnO_2$ aerogel is characterized by the scanning electron microscope (SEM) to investigate the morphology, and ultraviolet–visible–near infrared (UV–vis–NIR) and Fourier-transform infrared (FTIR) spectroscopy are employed for the optical absorbing performances. The SEM image of the MnO_2 nanoparticle, as shown in Figure S1 (Supporting Information), illustrates that the MnO_2 nanoparticles have a typical size smaller than 1 µm, indicating it can help improve the porous structure of the cellulose hydrogel to be mixed with.[46] It can be verified that introducing the MnO_2 nanoparticles indeed helps increase the porosity of the pristine cellulose. The comparison of the surfaces of the pristine cellulose and MnO_2 doped cellulose illustrates that MnO_2 nanoparticles introduce a rough and porous structure into the pristine cellulose substrate, which is relatively smooth, as shown in Figure 2b,c, respectively. The improved porosity not only increases the surface-to-volume ratio of the $NCC-MnO_2$ nano-composite that allows better adsorption and transportation of water inside the hydrogel but also enhances the light trapping effect due to the scattering and diffused reflection inside these nanopores. This will help enhance the overall light absorption performance and the water evaporation efficiency.[47]

The UV–vis-NIR spectrum shows the different absorption behaviors of the loaded MnO_2 and LIG solar absorbers, as shown in Figure S2 (Supporting Information). While the MnO_2-loaded NCC aerogel tends to have higher absorption at visible and short-wavelength portion of the solar spectrum, the LIG covers more on the longer wavelength, so these two materials compensate each other when integrated together to have a full-spectrum solar absorber for higher absorbing efficiency. For the IR light within the 2.5 µm to 25 µm range, these two materials have a significant enhancement of the absorption ability compared to the pristine cellulose substrate, as shown in Figure S3. Therefore, the composite $NCC-MnO_2$-LIG materials work together to form an excellent solar light absorber and water evaporator.

The directly laser-transferred LIG is superhydrophobic due to the oxygen-lacking atmosphere when the transferred LIG is induced from the bottom side of the polyimide film. Researchers reported the successful modification of the hydrophilicity of LIG under different gas environments at the generation stage.[48] Therefore, a laser post-scribing on the directly transferred LIG can also change the surface structures and the hydrophilicity of the LIG since the LIG is exposed to air, and the impact of the laser pulses can deform the morphology to some extent. The SEM images of the freshly transferred LIG and the laser post-scribed LIG reflect that the freshly prepared LIG tends to have larger pores and sparse pore distribution. In contrast, the LIG after laser post-scribing delivers denser but smaller pore sizes, indicating that the surface morphology has been successfully modified by the laser post-scribing process, as shown in Figure 2d,e, respectively. Therefore, the water wettability of these two types of LIG is different.

The hydrophilicity of the LIG used for the evaporator is investigated by the contact angle measurement. The pristine cellulose itself is superhydrophilic with a contact angle of nearly 0° that can hardly be acquired from the contact angle measurement, as shown in Figure S4a (Supporting Information). However, the directly laser-transferred LIG deposited without post-scribing is superhydrophobic with a contact angle of 151.8°. In contrast, the LIG with post-scribing is superhydrophilic with a contact angle of around 7.1°, as shown in Figure S4b,c (Supporting Information), respectively.

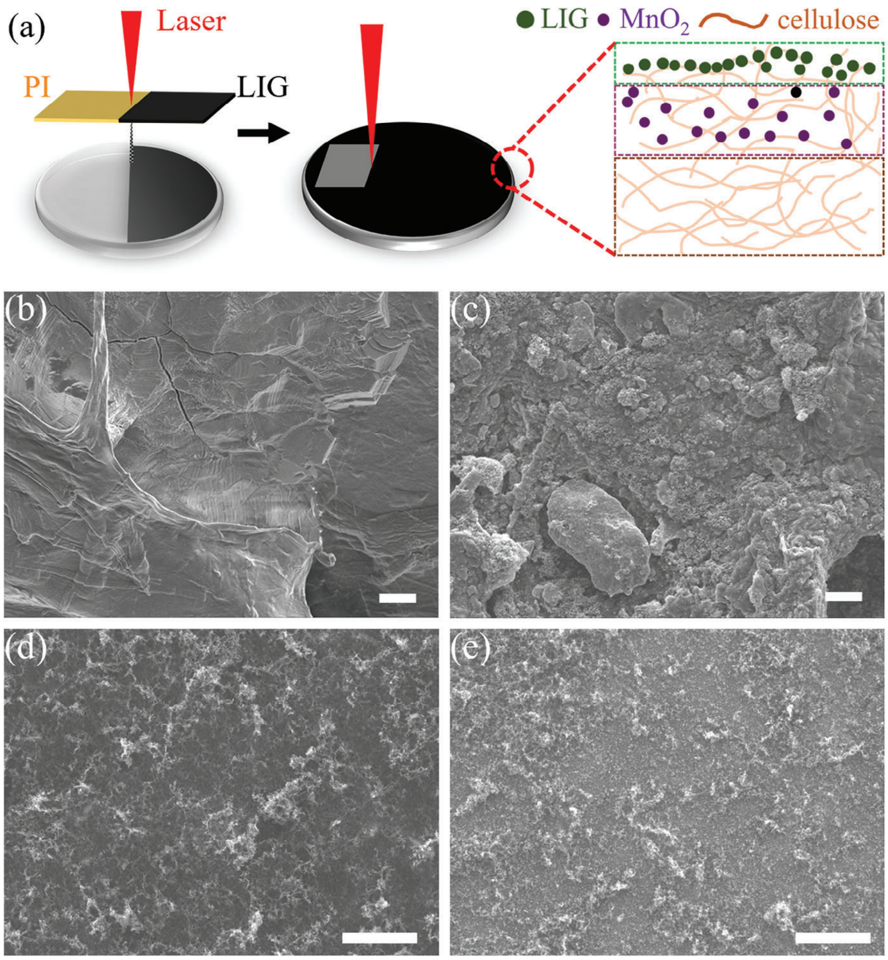

Figure 2. a) The illustration of the synthesis and fabrication of the three-layer composite NCC-MnO_2-LIG hydrogel evaporator with laser transferring and laser post-scribing. The SEM images of the b) pristine cellulose with a smooth surface and c) cellulose-MnO_2 composite with a rough and porous surface. The SEM images of the d) freshly transferred LIG with sparse and large pores and e) LIG after laser post-scribing with dense and small pores. Scale bars in (b) and (c) are 10 µm. Scale bars in (d) and (e) are 100 µm.

2.2. Electrical Impedance Tomography (EIT) Monitoring of Salt Transportation

The electrical impedance tomography technique is employed to monitor the saline water transportation inside the hydrogel evaporator network during the solar evaporation process. We build a 32-electrode EIT measurement device with a home-designed printed circuit board (PCB) to collect and analyze the data with home-developed programs. The EIT electrodes are made of stainless steel which are highly resistant to the corrosion of the seawater.[49] The EIT PCB can transmit the data to the computer via Bluetooth so that it will not interfere with the evaporation system and avoid any fluctuations caused by mechanical disturbance.

2.2.1. Verification of EIT Detection for Saline Distribution

A few tests were conducted to verify the feasibility and sensing performances of the EIT detection for the saline water before the application to evaporation. First, it is confirmed that the EIT detection device can successfully distinguish between saline and fresh water and accurately reveal the position of the saline drops when dropped into the DI water as the background medium. As shown in **Figure** 3a,b, the EIT electrodes are inserted in a container with DI water. Three drops of 3.5 wt% NaCl solution with 20 µL volume are dropped into the EIT detection container sequentially. The EIT sensing device immediately reflects the accurate positions of the three saline drops in the correct order of being added into the DI water, as shown in the increasing number of marked circles in Figure 3(c1–c3). In these EIT detection images, cool colors like blue mean higher electrical conductivity, while warm colors like red mean lower electrical conductivity. Since DI water barely contains ions, most of the region is green, while only three spots corresponding to the location where the saline drops are added are in deep blue. This proves that the EIT detection is capable of telling apart the saline water from the low-conductive background DI water.

A further investigation was carried out for the EIT detection sensitivity at different saline concentrations and the detection lower bound. Three drops of saline water (3.5 wt% NaCl solution)

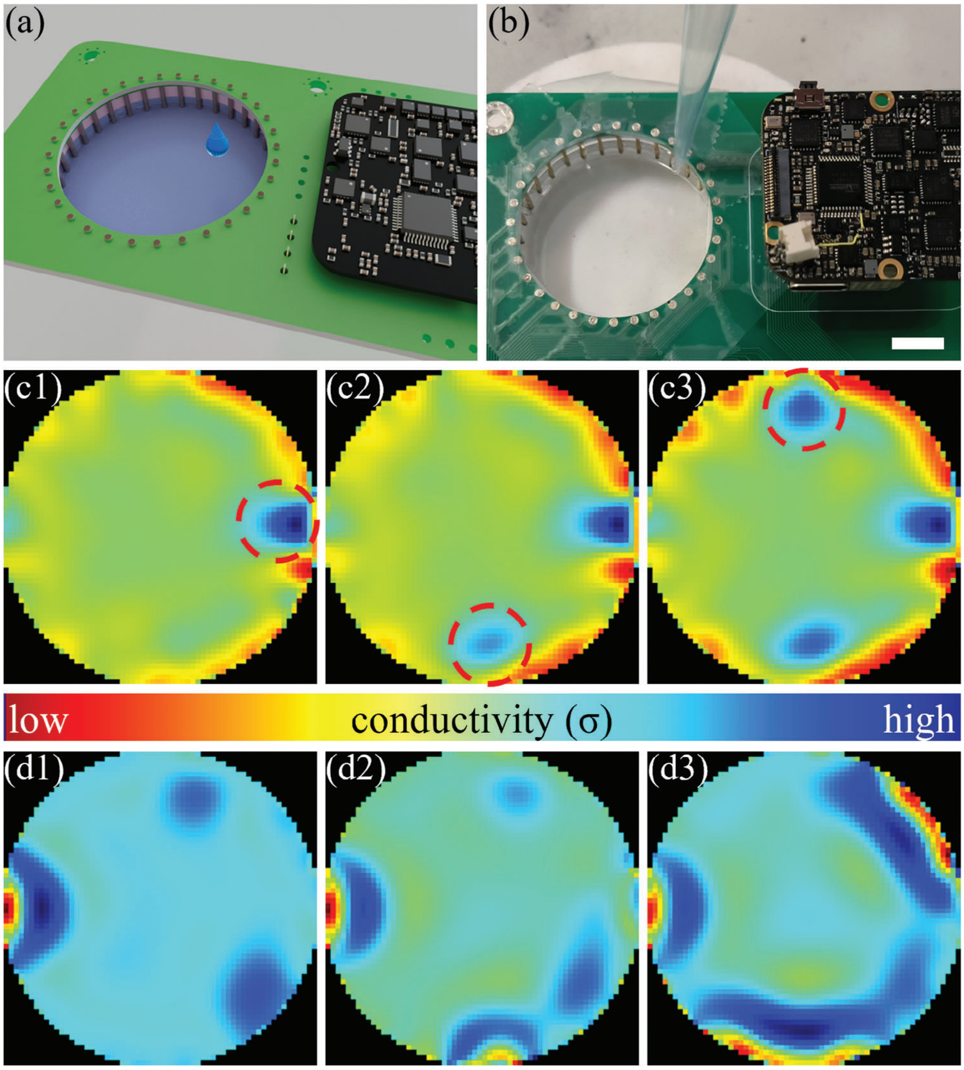

Figure 3. The a) illustration and b) photo of the NaCl saline dropped into the EIT detecting device with a home-designed PCB. c) The EIT detection images for the three added saline drops in consequence. d) The EIT detection images for the diffusion of the added saline drops at a time interval of 20 s. Scale bar in (b) is 1 cm.

are added in the order of concentration of 0.5 wt%, 1 wt%, and 2 wt% into the pristine cellulose hydrogel, as shown in Figure S5a (Supporting Information). The EIT-detected images were taken starting from the zero-concentration status in the order of adding the saline drops. From Figure S5b (Supporting Information), we can observe that the EIT images report a clear signal of the existence of saline drops when the 1 wt% saline is added. However, there are no obvious signal differences between the background and the 0.5 wt% saline drops. Therefore, we believe this EIT sensing device can detect the lower bound of 1 wt% saline concentration.

The above two tests were conducted at static and transient states, which means that the EIT images were taken immediately after the saline drop was added, and the changes over time were not recorded. It is also crucial to confirm the ability of the EIT detection in a continuous detection duration because it is a more common and necessary case for the long-time solar-driven water evaporation process. Therefore, we added the 3.5 wt% NaCl drops onto thin cellulose hydrogel and let the EIT detection device continuously record the EIT signals. The EIT signals are taken at an interval of 1 min. In the beginning period, we can observe clear boundaries of the deep blue spots representing the dropped NaCl solution. The distances between EIT signal spots are also far as the drops are added separately for better distinguishment, as shown in Figure 3d1. However, as time goes on, the previously clear boundaries start to become blur and the area of the blue spots are expanding, as shown in Figure 3d2. Eventually, the boundaries between the EIT signal spot gradually vanish so that some spots are even connected with neighboring spots, as shown in Figure 3d3. We attribute this phenomenon to the diffusion of the saline water in the relatively thin cellulose hydrogel so that the salt ions can be transported together with water flow and be able to pass through the cellulose hydrogel molecular network. This result proves that the EIT electrodes can indeed detect salt transportation without the interference of the water flow. It also reminds us to adjust the water concentration of the

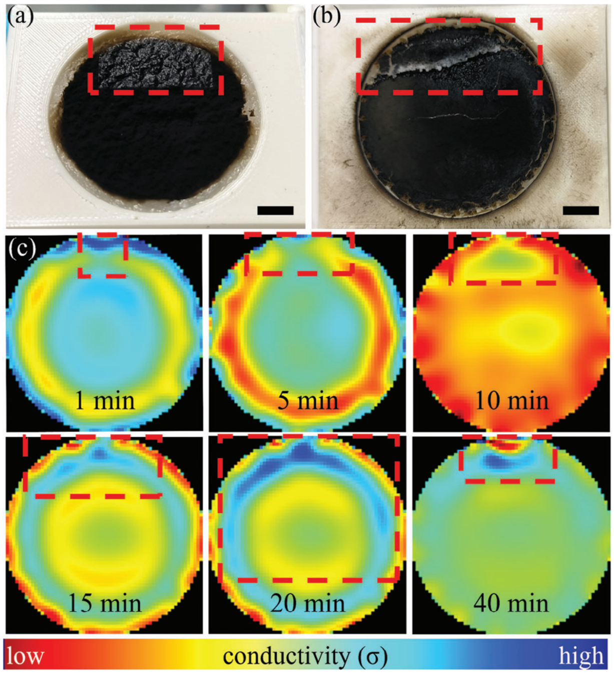

Figure 4. a) The photo of the laser-transferred superhydrophobic LIG and laser post-scribed superhydrophilic LIG. b) The photo of the superhydrophilic LIG window with salt crystals observed after 8 h of evaporation under light illumination. c) The EIT images of the completed NCC-MnO_2-LIG evaporator under simulated solar light recorded at 1 min, 5 min, 10 min, 15 min, 20 min, and 40 min. Scale bars in (a) and (b) are 1 cm.

cellulose-MnO_2 hydrogel to a suitable condition for solar-driven evaporation when the EIT monitoring is in detection.

2.2.2. EIT-Guided Optimization for Evaporator Design

A solar-drive evaporation test lasting for 8 h further proves the accuracy of the EIT detection and its ability to tell small amounts of saline concentration changes before any actual precipitation of solid salt crystal. We deposit the LIG onto the top surface of the NCC-MnO_2 hydrogel to form the superhydrophobic LIG majority. Then, we select a small window area in a rectangular shape and perform the laser post-scribing to turn the superhydrophobic LIG into superhydrophilic LIG, as shown in Figure 2a. After the stabilization process, when the aerogel absorbs water via the capillary effect, the successful reverse of the hydrophilicity of the LIG coating can be confirmed by the water-wetting status on the surface, where only the superhydrophilic LIG window is wetted by the water transported by the cellulose network from the bottom saline water reservoir, as shown in **Figure** 4a.

The evaporation apparatus with this superhydrophilic LIG window is kept under the simulated solar lamp for 8 consecutive hours with the EIT signals recorded during the first 1 h. As shown in Figure 4b, it is observed that only the superhydrophilic LIG window area caused the accumulation of salt crystal after 8 h of solar light illumination. In contrast, the other area is still clean and free of salt crystals. It indicates that the superhydrophilic area provides a suitable transportation channel for salt water so that it can be transported to the surface, and the water is rapidly evaporated, leaving the salt to be concentrated and finally turned into salt crystals. At the same time, the superhydrophobic LIG can inhibit the formation of salt crystals.

The EIT images help to verify the above hypothesis with the observation of the high conductivity area, which corresponds to the high concentration saline flow, as shown in Figure 4c, which is recorded in different time points in the first 1 h. The EIT electrodes send the probing current signals to the cellulose hydrogel and receive the voltage signals. The LIG coating with high resistance due to its loose connection and porous structures has little contribution to the EIT signals. We can verify it from the time evolution of the electrical conductivity distribution in the EIT images. At the very beginning of solar evaporation, the EIT signal shows an increased conductivity spot at the superhydrophilic LIG evaporation window area. As the evaporation time goes on, more and more salt is transported toward the superhydrophilic LIG window. Thus, the conductivity from the EIT images is getting higher and higher, as marked by the area of the red frame boxes in Figure 4c. It can also be determined that the saline results in a concentration gradient that peaks at the evaporation window and gradually decreases away from the window, which can concluded from the EIT images at the 15th and the 20th minute. At the end of the first hour, the EIT image shows that the saline concentration at the evaporation site is sufficiently high so that other areas show a relatively flat concentration profile. These EIT signals reveal the underlying salt transportation process. The saline is gradually transported to the superhydrophilic LIG area very quickly after the solar light illumination is on before the crystallization of solid salt builds up so intensely that it can be seen. It enlightens us that the salinity can be guided by the engineering of the hydrophilicity of the evaporator interface due to the evaporation-induced matter flow.

As a final result, we proposed to apply an indented pattern of superhydrophilic/superhydrophobic LIG surface coating as the optimized photothermal layer as the previous results show that the water can be evaporated via the superhydrophilic area while the superhydrophobic area helps inhibit the accumulation of salt crystals. The indented pattern is shown in Figure S6a (Supporting Information) in which the black area is for the laser induction of superhydrophobic LIG while the grey area is for the laser post-scribing of superhydrophilic LIG, as shown in Figure S6b (Supporting Information). The evaporation rates of such indented wettability evaporators are recorded by the mass loss under the solar simulator, as shown in Figure S6c (Supporting Information). The evaporation efficiency for the indented evaporator is 1.51 $kgm^{-2}h^{-1}$, with the background value of 0.53 $kgm^{-2}h^{-1}$ for open water condition. What is more, we found the evaporation rates for evaporators with different numbers of blotting paper as the water transportation channels are not highly sensitive to the numbers of water transportation channels, indicating that one piece of blotting paper can provide sufficient water supply, as shown in Figure S7 (Supporting Information).

2.3. Bacteria Test of the Condensed Clean Water

A bacteria cultivation test is conducted with raw seawater and the collected clean water collected by condensation from evaporation

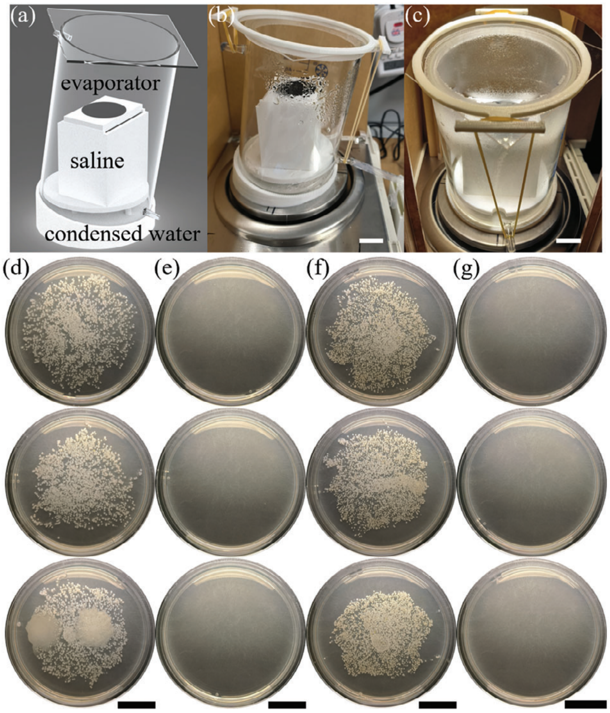

Figure 5. The a) illustration and the b) side view and c) front view of the device to collect the condensed water from the solar-driven evaporator. The bacterial colony of d) the *Escherichia coli*-polluted seawater and e) the corresponding condensed water, and f) the *Staphylococcus aureus*-polluted seawater and g) the corresponding condensed water. Scale bars in (b–g) are 2 cm.

to confirm that this evaporator can effectively remove the bacteria in the polluted water and generate clean water.

The collection of the condensed water is quite crucial to the solar-driven water evaporation as the ultimate target is to convert the evaporated water vapor into liquid fresh water, where good design of the collection device can greatly benefit the evaporation.[50] The collection device is made of a glass beaker with a highly transparent quartz plate as the covering top to permit solar light to penetrate and collect the condensed water on the rooftop, as shown in **Figure 5a**. The quartz plate has a thickness of 1 mm to reduce the loss of the sunlight when passing through it. What is more, the quartz plate is treated with the O-plasma on the surface to make it more hydrophilic so the condensation of water droplets on it will be easier. The hydrophilicity of the rooftop has significant influences on the water condensation process, as can be shown in Figure S8 (Supporting Information). The photo of the acrylic plate with a contact angle of around 90.6° shows much worse water condensation conditions with large droplets while the hydrophilic quartz plate with a contact angle of around 5.5° delivered much better condensation results during the same evaporation time. The saline water reservoir container and the NCC-MnO_2-LIG evaporator are placed inside the glass beaker under the solar light illumination. The condensed water is guided into a glass nozzle at the bottom of the glass beaker and then is collected by a clean tube, as shown in Figure 5b,c. All the equipment involved is sterilized and dried to eliminate the remaining bacteria or contamination.

We confirm the bacteria colonies in the raw seawater freshly sampled from the seashore on campus. The raw seawater is added to the agar plates for incubation without dilution, and the colonies are shown in Figure S9a (Supporting Information). Since the raw seawater can only deliver very few colonies, indicating the concentration of bacteria in raw seawater is limited, we choose *Escherichia coli* (*E. coli*) and *Staphylococcus aureus* (*S. aureus*) as the testing species for more observable results. The *E. coli* and *S. aureus* suspension is added into the seawater at the concentration of 2 % to form the simulated polluted saline. The bacteria colony incubation test shows that the bacteria can live and reproduce generally in the seawater environment, as confirmed by Figure S9b,c (Supporting Information) for the *E. coli* and *S. aureus*, respectively. The simulated polluted saline is then put under the solar simulator lamp for evaporation using the proposed NCC-MnO_2-LIG hydrogel evaporator. The collected condensed water after 8 h of light illumination is put on the agar plates for 18 h of incubation.

The simulated polluted saline without the evaporation procedure delivers a significant number of colonies for both *E. coli* and *S. aureus*, as shown in Figure 5d,f, respectively. However, no colony is observed for either the *E. coli* or *S. aureus* from the collected condensed water, which proves that the NCC-MnO_2-LIG hydrogel evaporator successfully removes the bacteria in the polluted water, as shown in Figure 5e,g, respectively. This result is at the same quality or better than the reference evaporators which have 100 % or less anti-bacterial efficiency.[51–54] The anti-bacterial tests prove that this solar-driven NCC-MnO_2-LIG hydrogel evaporator can efficiently remove the contamination in the polluted saline water and generate fresh and clean water.

3. Conclusion

In this work, we propose a cellulose-based hydrogel evaporator doped with MnO_2 nanoparticles and coated with the LIG layers as the solar light photothermal absorber for the solar-driven desalination based on evaporation to generate fresh and clean water. The laser engineers the LIG layer to have a superhydrophobic and superhydrophilic wettability. We innovatively applied the electrical impedance tomography technology to observe the behaviors of solutes before and near precipitation during the solar evaporation process by a home-designed EIT device implanted in the cellulose network hydrogel in real-time. Particularly noteworthy is the detailed graphic illustration of the invisible salt transportation process and its feedback loop for guiding the design using the laser-engineered superhydrophobic/superhydrophilic LIG surface coating, as we confirm that the hydrophilicity of the evaporator surface can significantly affect the salt crystallization process. The safety of the condensed water evaporated by our NCC-MnO_2-LIG hydrogel evaporator is verified as it delivered absolutely no bacteria colony in the bacteria incubation test. We hope this work could shed light on further research about the anti-salt solar-driven desalination for people with water crises around the world.

4. Experimental Section

Materials: The nano-crystal cellulose was from NanoFC, Zhongshan, China. The MnO_2 nanoparticle is from Brofos Nano Technology, Ningbo, China. NaCl is from CLS, HKUST. The PI film (50 µm thick) was from Chenxi Electronics Technology, Dongguan, China.

Fabrication of Cellulose Hydrogel: The NCC precursor was sonicated with an ultrasonic cell crusher (ATPIO, China) for 10 min with a sonication duty cycle of 33 %. Then the NCC precursor was mixed with MnO_2 powder with mass concentration of 1 wt% and was shaken intensely for 5 min and then sonicated for 10 min with duty cycle of 33 % to make sure the NCC precursor and the MnO_2 powder were mixed sufficiently for a homogeneous mixture. The NCC-MnO_2 mixture was poured into the 3D-printed evaporation device mold and formed a flat and smooth surface before being sent to the refrigerator for 2 h. The frozen samples and devices were put into the freeze-dryer (LC-10N-50A) for 24 h of freeze-drying. After that, the NCC-MnO_2 became the cellulose aerogel.

Preparation of the Solar Absorber: After the freeze-dried NCC-MnO_2 aerogel was prepared, the samples were taken out and let the bottom surface touch the water for 15 min of relaxation to allow the aerogel to absorb water naturally and became the NCC-MnO_2 hydrogel again. Then laser-induced graphene (LIG) was deposited on the top of the moist NCC-MnO_2 hydrogel with twice deposition.

Fabrication of Laser-Induced Graphene (LIG) Samples: A pulsed laser marking machine with a working wavelength of 1064 nm was used as the laser source. The laser parameters for the LIG induction applied with the on-focus condition are listed here: scanning speed (280 mm s^{-1}), power (9.6 W), filling line gap (10 µm), and repetition rate (100 kHz). Two pieces of PI film of the same size ware used and stuck on a hollow supporting frame so the LIG could fall onto the top of the hydrogel sample without introducing other contamination.

Fabrication of Superhydrophilic Area in LIG Samples: A second round of laser scribing was applied on the superhydrophobic side of the laser transfer-fabricated LIG layer under the on-focus condition using the listed parameters here: scanning speed (1000 mm s^{-1}), power (3 W), filling line gap (10 µm), and repetition rate (20 kHz).

Evaporation Test with EIT Device: A 3D-printed container with raw seawater and simulated polluted seawater (raw seawater with bacteria suspension of 2 % added) was used as the saline reservoir for solar-driven evaporation. The cellulose-MnO_2 was filled by a piece of water transporting blotting paper with 1 cm by 10 cm size to transport the bottom saline water continuously. The evaporator was then put on top of the seawater container under the solar simulator for evaporation and EIT monitoring.

Supporting Information

Supporting Information is available from the Wiley Online Library or from the author.

Acknowledgements

The work described in this paper was mainly supported by the funding of the Hong Kong Research Grants Council (25201620, C6001-22Y, and JLFS/P-603/24) and the Hong Kong Innovation and Technology Commission (ITC) under project No. MHP/060/21. The authors would also like to express their sincere thanks to the support from the State Key Laboratory of Advanced Displays and Optoelectronics Technologies at HKUST.

Conflict of Interest

The authors declare no conflict of interest.

Data Availability Statement

The data that support the findings of this study are available from the corresponding author upon reasonable request.

Keywords

electrical impedance tomography, laser-induced graphene, solar evaporation, salt transportation

Received: December 18, 2024

---

[1] S. Dutta, R. F. de Luis, J. Goscianska, A. Demessence, R. Ettlinger, S. Wuttke, *Adv. Funct. Mater.* **2023**, 2304790.
[2] M. Qasim, M. Badrelzaman, N. N. Darwish, N. A. Darwish, N. Hilal, *Desalination* **2019**, *459*, 59.
[3] Y. Song, M. Zeng, X. Wang, P. Shi, M. Fei, J. Zhu, *Adv. Mater.* **2024**, *36*, 2209134.
[4] S. Gorjian, H. Ebadi, in *Photovoltaic Solar Energy Conversion*, (Eds.: S. Gorjian, A. Shukla), Academic Press, Cambridge **2020**, pp. 1–26, ISBN 978-0-12-819610-6, https://www.sciencedirect.com/science/article/pii/B9780128196106000016.
[5] X. Yin, R. Yang, G. Tan, S. Fan, *Science* **2020**, *370*, 786.
[6] P. Tao, G. Ni, C. Song, W. Shang, J. Wu, J. Zhu, G. Chen, T. Deng, *Nat. Energy* **2018**, *3*, 1031.
[7] X. Wu, Y. Lu, X. Ren, P. Wu, D. Chu, X. Yang, H. Xu, *Adv. Mater.* **2024**, *36*, 2313090.
[8] S. C. Singh, C. Guo, *EcoMat* **2022**, *4*, e12161.
[9] S. Chen, Z. Sun, W. Xiang, C. Shen, Z. Wang, X. Jia, J. Sun, C.-J. Liu, *Nano Energy* **2020**, *76*, 104998.
[10] G. Li, W.-C. Law, K. C. Chan, *Green Chem.* **2018**, *20*, 3689.
[11] Y. Peng, W. Zhao, F. Ni, W. Yu, X. Liu, *ACS Nano* **2021**, *15*, 19490.
[12] M. Ding, H. Lu, Y. Sun, Y. He, J. Yu, H. Kong, C. Shao, C.-Y. Liu, C. Li, *Adv. Sci.* **2022**, *n/a*, 2205202.
[13] X. Li, Y. Tian, P. Zhang, N. Liu, H. Zhai, J. Ji, S. Zhao, Y. Liu, D. Xu, F. Wang, Y. Wei, L. Feng, *Adv. Funct. Mater.* **2023**, *33*, 2302019.
[14] B. Naghdi, F. Arabpour Roghabadi, A. Soleimani-Gorgani, *Desalination* **2024**, *577*, 117390.
[15] T. A. Cooper, S. H. Zandavi, G. W. Ni, Y. Tsurimaki, Y. Huang, S. V. Boriskina, G. Chen, *Nat. Commun.* **2018**, *9*, 5086.
[16] Z. Zhu, H. Zheng, H. Kong, X. Ma, J. Xiong, *Nature Water* **2023**, *1*, 790.
[17] H. Ghasemi, G. Ni, A. M. Marconnet, J. Loomis, S. Yerci, N. Miljkovic, G. Chen, *Nat. Commun.* **2014**, *5*, 4449.
[18] G. Ni, G. Li, S. V. Boriskina, H. Li, W. Yang, T. Zhang, G. Chen, *Nat. Energy* **2016**, *1*, 1.
[19] H.-S. Guan, T.-T. Fan, H.-Y. Bai, Y. Su, Z. Liu, X. Ning, M. Yu, S. Ramakrishna, Y.-Z. Long, *Carbon* **2022**, *188*, 265.
[20] Z. Wei, J. Wang, S. Guo, S. C. Tan, *Nano Res. Energy* **2022**, *1*, e9120014.
[21] M. Kim, K. Yang, Y. S. Kim, J. C. Won, P. Kang, Y. H. Kim, B. G. Kim, *Carbon* **2020**, *164*, 349.
[22] S. Luo, Z. Li, X. Cui, Y. Ge, *Chem. Eng. J.* **2023**, *454*, 140286.
[23] Y.-Z. Chen, H.-C. Yang, H.-N. Li, J.-H. Xin, C. Zhang, L.-S. Wan, Z.-K. Xu, *Small* **2024**, *20*, 2310952.
[24] H. Li, W. Zhang, X. Liao, L. Xu, *Sci. Adv.* **2024**, *10*, 26eado1019.
[25] X. Wu, Y. Wang, P. Wu, J. Zhao, Y. Lu, X. Yang, H. Xu, *Adv. Funct. Mater.* **2021**, *31*, 342102618.
[26] C. Gu, Y. Luo, K. Xu, A. Zhang, Z. Luo, L. Wang, *Adv. Sustainable Syst.* **2024**, *n/a*, 2400558.
[27] H.-N. Li, C. Zhang, J.-H. Xin, Y.-W. Liu, H.-C. Yang, C.-Y. Zhu, C. Liu, Z.-K. Xu, *ACS Nano* **2024**, *18*, 2434.
[28] Y. Wang, X. Wu, P. Wu, H. Yu, J. Zhao, X. Yang, Q. Li, Z. Zhang, D. Zhang, G. Owens, H. Xu, *J. Mater. Chem. A* **2022**, *10*, 14470.
[29] S. Zhang, M. Li, C. Jiang, D. Zhu, Z. Zhang, *Adv. Sci.* **2024**, *11*, 2308665.

[30] L. Li, C. Xue, Q. Chang, X. Ren, N. Li, J. Yang, S. Hu, H. Xu, *Adv. Mater.* **2024**, *36*, 2401171.
[31] C. Liu, Y. Peng, X. Zhao, *Carbohydr. Polym.* **2021**, *273*, 118536.
[32] S. W. Sharshir, A. M. Algazzar, K. A. Elmaadawy, A. W. Kandeal, M. R. Elkadeem, T. Arunkumar, J. Zang, N. Yang, *Desalination* **2020**, *491*, 114564.
[33] T. Zhang, S. Jiao, J. Zhao, G. Gao, Y. Yang, C. Guo, *Desalination* **2022**, *527*, 115576.
[34] X. Xu, Q. Zhao, Q. Liu, J. Qiu, J. Li, W. Zheng, J. Cao, L. Wang, W. Wang, S. Yuan, A. Fu, H. Yang, C. Wang, J. Xu, B. Lu, *Desalination* **2024**, *577*, 117400.
[35] X. Su, D. Hao, M. Sun, T. Wei, D. Xu, X. Ai, X. Guo, T. Zhao, L. Jiang, *Adv. Funct. Mater.* **2022**, *32*, 2108135.
[36] B. Zhang, P. W. Wong, A. K. An, *Chem. Eng. J.* **2022**, *430*, 133054.
[37] W. Q. Yang, L. Peng, *Meas. Sci. Technol.* **2002**, *14*, R1.
[38] H. Zhong, X. Lu, R. Yang, Y. Pan, J. Lin, M. Kim, S. Chen, M. G. Li, *Adv. Sci.* **2024**, 2406905.
[39] J. Chen, L. Xu, Z. Cao, H. Zhou, *IEEE Trans. Instrum. Meas.* **2014**, *63*, 432.
[40] X. Lu, S. Sun, K. Liu, J. Sun, L. Xu, *IEEE J. Biomed. Health. Inf.* **2022**, *26*, 2515.
[41] S. Sun, X. Lu, L. Xu, Z. Cao, J. Sun, W. Yang, *IEEE Trans. Instrum. Meas.* **2021**, *70*, 1.
[42] M. Tang, H. Zhong, X. Lu, R. Yang, C. K. W. Lee, Y. Pan, Y. Chen, M. G. Li, *Adv. Sci.* **2024**, *11*, 2402676.
[43] M. Tang, R. Yang, J. Lin, X. Lu, C. Kong Wai Lee, Y. Xu, S. Chen, H. Zhong, Y. Pan, M. G. Li, *Chem. Eng. J.* **2024**, *497*, 154880.
[44] Y. Wei, W. Li, S. Zhang, J. Yu, Y. Tang, J. Wu, S. Yu, *Adv. Funct. Mater.* **2024**, *n/a*, 2401149.
[45] H. Mahbub, M. A. Saed, M. Malmali, *ACS Appl. Mater. Interfaces* **2023**, *15*, 18074.
[46] L. Shu, X.-F. Zhang, Z. Wang, J. Liu, J. Yao, *Carbohydr. Polym.* **2024**, *327*, 121695.
[47] T. Arunkumar, J. Wang, D. Denkenberger, *Renewable Sustainable Energy Rev.* **2021**, *138*, 110547.
[48] A. Dallinger, F. Steinwender, M. Gritzner, F. Greco, *ACS Appl. Nano Mater.* **2023**, *6*, 16201.
[49] E. Husain, T. N. Narayanan, J. J. Taha-Tijerina, S. Vinod, R. Vajtai, P. M. Ajayan, *ACS Appl. Mater. Interfaces* **2013**, *5*, 4129.
[50] S. Guo, Y. Zhang, S. C. Tan, *Device* **2023**, *1*, 100099.
[51] L. Huang, L. Ling, J. Su, Y. Song, Z. Wang, B. Z. Tang, P. Westerhoff, R. Ye, *ACS Appl. Mater. Interfaces* **2020**, *12*, 51864.
[52] J. Zhang, Z. Li, T. Meng, S. Zang, C. Yang, X. Luo, H. Wang, J. Chen, F. Jing, C. Wang, H. Xu, Y. Zhou, *Chem. Eng. J.* **2022**, *450*, 137893.
[53] X. Chen, N. Yang, Y. Wang, H. He, J. Wang, J. Wan, H. Jiang, B. Xu, L. Wang, R. Yu, L. Tong, L. Gu, Q. Xiong, C. Chen, S. Zhang, D. Wang, *Adv. Mater.* **2021**, *34*, 2107400.
[54] J. Xie, X. Wang, J. Lin, S. Kong, H. Lu, Z. Liu, Q. Wang, J. Zuo, F. Hu, Z. Zeng, *Chem. Eng. J.* **2024**, *497*, 154771.